European Journal of Soil Science

European Journal of Soil Science, April 2011, **62**, 305–317 doi: 10.1111/j.1365-2389.2010.01328.x

Biogeochemical processes and arsenic enrichment around rice roots in paddy soil: results from micro-focused X-ray spectroscopy

J. Frommer[a], A. Voegelin[b], J. Dittmar[a], M. A. Marcus[c] & R. Kretzschmar[a]

[a]*Soil Chemistry Group, Institute of Biogeochemistry and Pollutant Dynamics, Department of Environmental Sciences, ETH Zurich, CHN, CH-8092 Zurich, Switzerland,* [b]*Eawag, Swiss Federal Institute of Aquatic Science and Technology, Überlandstrasse 133, CH-8600 Dübendorf, Switzerland, and* [c]*Advanced Light Source, Lawrence Berkeley National Laboratory, 1 Cyclotron Road, Berkeley, CA 94720, USA*

Summary

The spatial distribution and speciation of iron (Fe), manganese (Mn) and arsenic (As) around rice roots grown in an As-affected paddy field in Bangladesh were investigated on soil sampled after rice harvest. Synchrotron micro-X-ray fluorescence spectrometry on soil thin sections revealed that roots influence soil Fe, Mn and As distribution up to 1 mm away from the root–soil interface. Around thick roots (diameter around 500 μm), Mn was concentrated in discrete enrichments close to the root surface without associated As, whereas concentric Fe accumulations formed farther away and were closely correlated with As accumulations. Near thin roots (diameter < 100 μm), in contrast, a pronounced enrichment of Fe and As next to the root surface and a lack of Mn enrichments was observed. X-ray absorption fine structure spectroscopy suggested that (i) accumulated Fe was mainly contained in a two-line ferrihydrite-like phase, (ii) associated As was mostly As(V) and (iii) Mn enrichments consisted of Mn(III/IV) oxyhydroxides. The distinct enrichment patterns can be related to the extent of O_2 release from primary and lateral rice roots and the thermodynamics and kinetics of Fe, Mn and As redox transformations. Our results suggest that in addition to Fe(III) plaque at the root surface, element accumulation and speciation in the surrounding rhizosphere soil must be taken into account when addressing the transfer of nutrients or contaminants into rice roots.

Introduction

In Bangladesh and West Bengal large areas of paddy soils are irrigated with groundwater for the production of dry season (*boro*) rice. Because the water from shallow tube wells often contains large concentrations of toxic arsenic (As), intensive irrigation may result in the accumulation of As in paddy soils (Dittmar *et al*., 2007), which jeopardizes both rice quality and yield (Panaullah *et al*., 2009). Arsenic uptake by rice plants occurs *via* a variety of different biochemical pathways depending on the plant genotype, the chemical form of As and the prevailing environmental factors (Zhao *et al*., 2009). As well as the biochemical transfer across the soil-root interface, the transport of As through the rhizosphere to the root surface is also crucial for the bioavailability of As for plants. Thus, knowledge of the biogeochemical processes affecting As transport towards roots is needed to improve the mechanistic understanding of the transfer of As from paddy soil into rice plants.

Because rice roots aerate themselves internally and release molecular oxygen (O_2) into the rhizosphere soil (Revsbech *et al*., 1999; Kirk, 2003), the distribution, speciation and bioavailability of redox sensitive elements such as iron (Fe), manganese (Mn) and As are controlled by the gradients developing between the periodically anoxic soil matrix, the partly aerated rhizosphere, and the O_2-releasing root surface (Fitz & Wenzel, 2002). In particular, the dominant oxidation state of these elements (Fe(II)/Fe(III) and As(III)/As(V)) changes along the redox gradient, which has a pronounced impact on their mobility and retention. In flooded soil, microbial respiration results in the mobilization of As into porewater via the reductive dissolution of Fe(III)-oxyhydroxide sorbent phases and *via* the reduction of As(V) to As(III), which exhibits less sorption affinity under typical soil chemical conditions (Weber *et al*., 2010). In line with these trends, extended soil flooding and anoxia enhance As uptake by rice compared with aerobically grown rice (Xu *et al*., 2008; Li *et al*., 2009). To some

Correspondence: A. Voegelin. E-mail: andreas.voegelin@eawag.ch

Received 23 December 2009; revised version accepted 23 September 2010

© 2010 The Authors
Journal compilation © 2010 British Society of Soil Science

extent, however, iron plaque forming on the surface of rice roots in reduced soil may sequester As and thereby counteract an otherwise enhanced uptake (Liu *et al*., 2006; Hossain *et al*., 2009; Zhao *et al*., 2009). The Fe plaque mainly consists of amorphous and short-range ordered Fe(III) precipitates such as ferrihydrite (Liu *et al*., 2006; Voegelin *et al*., 2007). The formation of Fe plaque follows the oxidation of Fe(II) to Fe(III) by O_2 released from the roots (Otte *et al*., 1995; Zhao *et al*., 2009). Concomitantly, As(III) is oxidized to As(V) (Roberts *et al*., 2004), which has a large affinity for Fe(III) precipitates in the plaque. Phosphate may lessen the sequestration of As by competing in coprecipitation and sorption reactions (Roberts *et al*., 2004; Hossain *et al*., 2009; Voegelin *et al*., 2010) as well as by inhibiting the formation of the Fe plaque (Liu *et al*., 2004). However, As may not only be sequestered by Fe plaque, but could also bind to Mn(III/IV) oxyhydroxides that may form around plant roots.

The majority of the studies addressing the retention of As in the rhizosphere were carried out in hydroponic cultures (Liu *et al*., 2004) or on roots separated from soil prior to investigation (Hansel *et al*., 2002; Liu *et al*., 2006; Hossain *et al*., 2009). Such experimental designs are ideally suited to study the Fe plaque adhering to the roots. However, they provide no insights into elemental distribution and speciation gradients in the rhizosphere soil. Distinct element enrichments related to root activity may form up to several hundreds of micrometres away from the root surface in salt marsh sediments and seasonally flooded soils (Caetano & Vale, 2000; Voegelin *et al*., 2007). In addition, rice plants develop a complex system of primary roots and branching fine lateral roots (Kirk, 2003). The O_2 fluxes to the rhizosphere (Armstrong, 1971) and possibly the release of exudates vary between the different root types, such that different micro-environments are expected to form.

To better understand the relation between soil As and the uptake of As by plants, studies on the root-associated Fe plaque need to be complemented by spatially resolved studies on the element speciation and distribution in the rhizosphere soil. The objectives of the present work were therefore to investigate the distribution and speciation of Fe, Mn and As in the rhizosphere at the micrometer scale. Undisturbed soil samples and bulk soil were collected after rice harvest on a paddy field irrigated with As-rich groundwater (Roberts *et al*., 2007). The field site has been thoroughly characterized in previous work with respect to the Fe, Mn and As dynamics in both the soil and the pore water throughout the annual cycle of irrigation and monsoonal flooding (Dittmar *et al*., 2007; Roberts *et al*., 2007, 2009; Roberts, 2009). We focused not only on As but also on Fe and Mn, because the latter two elements form major sorbent phases for As and because their distribution and speciation provide information on redox conditions within the rhizosphere. The spatial distribution of Fe, Mn and As was analysed by micro-focused X-ray fluorescence (μ-XRF) spectrometry and their speciation was assessed by X-ray absorption fine structure (XAFS) spectroscopy. Complementary data on element speciation and fractionation in dried bulk soil was obtained by XAFS and a sequential chemical extraction, respectively.

Materials and methods

Collection and characterization of soil samples

Samples were taken from a rice field located near Sreenagar (Munshiganj district, Bangladesh), 30 km south of Dhaka. The field is irrigated by a single shallow tube well with water containing approximately 400 $\mu g\ l^{-1}$ As (Roberts *et al*., 2007) via a single irrigation water inlet, which resulted in decreasing soil As concentrations with increasing distance from the inlet (Dittmar *et al*., 2007). Total soil As concentrations increase as a result of irrigation in the dry season and decrease through As leaching during the monsoon (Dittmar *et al*., 2007). Pore water analyses showed that the dominant redox state in the topsoil changes from reducing at the time of rice transplantation to oxic conditions over the irrigation period, which has a pronounced impact on the levels of Fe, Mn and As exposed to the rice roots throughout the growth cycle (Roberts, 2009). Soil samples were collected close to the irrigation water inlet of a paddy field in May 2007 after rice harvest when the topsoil was aerated (field labelled 'G' in Dittmar *et al*., 2007). Bulk soil samples were collected with a core sampler (Dittmar *et al*., 2007). The soil cylinder spanning the depth between 5 and 10 cm (diameter, 3.5 cm) was used in this study. The sample was oven-dried in the laboratory at 60°C, ground to <0.2 mm, and homogenized. Total element composition was determined by energy-dispersive X-ray fluorescence spectrometry (XRF, Spectro X-Lab 2000, Spectro Analytical Instruments GmbH, Kleve, Germany).

The fractionation of Fe, Mn and As in the dried bulk soil was determined by using a sequential extraction (SE) scheme. The procedure included six extraction steps of a seven-step SE procedure (Zeien & Brümmer, 1989) to give the following fractions (solution-to-soil ratio (SSR) in ml g^{-1}; reaction time; hypothetical interpretation according to Zeien & Brümmer (1989)): F1, 1 M NH_4NO_3 (SSR = 25; 24 hours; readily soluble and exchangeable); F2, 1 M NH_4 acetate, pH 6.0 (SSR = 25; 24 hours; specifically sorbed, $CaCO_3$ bound, and other weakly bound species); F3, 0.1 M NH_2OH-HCl plus 1 M NH_4 acetate, pH 6.0 (SSR = 25; 30 minutes; Mn oxides); F4, 0.2 M NH_4 oxalate, pH 3.25, in dark (SSR = 25; 2 hours; amorphous and poorly crystalline Fe oxides); F5, 0.1 M ascorbic acid in 0.2 M NH_4 oxalate, pH 3.25, in boiling water (SSR = 25; 2 hours; crystalline Fe oxides); F6, XRF analysis (residual fraction). The extractions were performed in triplicate and the concentrations of Fe, Mn and As were measured using ICP-OES (CCD simultaneous ICP-OES, Vista-MPX, Varian, Australia). The sum of Fe, Mn and As extracted in F1 to F6 deviated by +1, +2% and −11% from total concentrations determined by XRF.

Undisturbed samples for the preparation of soil thin sections were taken at a depth between 0 and 10 cm near the sampling location of the bulk soil with Kubiena boxes (aluminum; 3.5 × 4 × 4 cm). The samples were immediately sealed in plastic bags, transported to the laboratory within 7 days, frozen by immersion in liquid N_2, and freeze-dried. The dried samples were embedded with LR White resin (London Resin, Reading, UK) under vacuum

© 2010 The Authors

followed by a 48-hour curing at 60°C in an 80 kPa N_2 atmosphere. Polished 30-μm thin sections were prepared on As-free glass support (Thomas Beckmann, Schwülper-Lagesbüttel, Germany).

Bulk X-ray absorption spectroscopy

For bulk XAFS spectroscopy at the Fe, Mn and As K-edges, about 100 mg of the soil sample was mixed with B_4C and wax and pressed into pellets (diameter, 1.3 cm). Arsenic and Mn K-edge X-ray absorption near edge structure (XANES) spectra were measured at the XAS beamline at the Angströmquelle Karlsruhe (ANKA, Karlsruhe, Germany). The beamline is equipped with a Si(111) double crystal monochromator (DCM), which was calibrated using metal foil spectra (first inflection points of Mn-foil K-edge XANES set to 6539 eV and of Au-foil L_3-edge XANES set to 11 919 eV, respectively). The soil pellet was measured at room temperature in fluorescence mode using a five-element Ge solid state detector. Spectral data processing and linear combination fitting (LCF) were performed using the software code Athena (Ravel & Newville, 2005). Spectra of As(V) and As(III) sorbed onto two-line ferrihydrite (Voegelin *et al*., 2007) served as references for As data analysis. References for Mn included 50 mM Mn^{2+} ($MnCl_2$), Mn in chlorite (source clay reference chlorite CCa-2 containing approximately 650 mg kg^{-1} Mn, mainly Mn(III)), and synthetic Na-birnessite.

The Fe K-edge spectrum of the bulk soil sample was measured on beamline BM01 (Swiss Norwegian Beamline, SNBL) at the European Synchrotron Radiation Facility (ESRF, Grenoble, France) in transmission mode using a Si(111) DCM, calibrated by setting the first inflection point of the Fe-foil K-edge XANES to 7112 eV. The EXAFS spectrum was extracted using the AUTOBK algorithm implemented in Athena. A Kaiser-Bessel apodization window with a sill width of 2 $Å^{-1}$ was used to Fourier transform the data over a k-range of 2.5–11 $Å^{-1}$. Twelve reference compounds for Fe(II) and Fe(III) in different structural environments (as listed in Table S1), were selected to cover a wide range of Fe coordination environments likely to occur in soils. These references were measured at the XAS beamline at ANKA and at beamlines A1 and C at the Hamburger Synchrotronstrahlungslabor (HASYLAB, Hamburg, Germany) using similar procedures as described above for the soil sample. To facilitate data interpretation, the reference compounds were classified into six groups according to their structural similarity. These groups were: Fe(II)-rich trioctahedral phyllosilicates, Fe(III)-rich dioctahedral phyllosilicates, Fe(III) (oxyhydr)oxides, carbonates, sulphides and aqueous Fe(II). LCF of the EXAFS spectrum of the soil sample with the 12 references was carried out by first adding the reference spectrum giving the smallest R-factor ($= \sum(\text{data}_i - \text{fit}_i)^2 / \sum \text{data}_i^2$). A best-fit procedure involving n + 1 components was only considered to be superior to the best n-component fit if the R-factor decreased by more than 10% (relative). The LCF was carried out with the k^3-weighted data over a k-range of 3–11 $Å^{-1}$ using software from the ALS beamline 10.3.2. The reference spectra selected by LCF of the EXAFS spectrum were subsequently used in a LCF of the smoothed first derivative XANES of the soil sample (E-range, 7108–7158 eV). The fractions of individual components were constrained to positive values.

Micro-focused X-ray analysis

The soil thin sections were analysed with micro-focused X-ray fluorescence spectrometry (μ-XRF) at beamline 10.3.2 at the Advanced Light Source (ALS, Berkeley, CA, USA). The speciation of Fe, Mn and As was probed at selected points of interest (POI) by μ-XANES (Fe, Mn and As) and μ-EXAFS (Fe) spectroscopy. The Fe μ-XAFS spectra were evaluated with the LCF approach outlined for the bulk XAFS spectra. The Mn and As spectra were evaluated qualitatively. (Additional information on the XAFS data reduction and evaluation as well as on the methods used for the collection and evaluation of the μ-XRF and μ-XAFS data can be found in the Supporting Information).

Results

Soil properties and element fractionation

The soil at the study site was carbonate free and had a silt loam to silty clay loam texture. In the soil profile characteristic redoximorphic features such as soil mottling were visible (Dittmar *et al*., 2007). Powder X-ray diffraction (XRD) showed mica, quartz, feldspar and a number of clay minerals (illite, chlorite, vermiculite and kaolinite) as being the main mineralogical constituents of the topsoil (Figure S1).

The total contents of Fe, Mn and As in the topsoil along with selected results from sequential extraction (SE) are summarized in Table 1. With 41 mg kg^{-1}, the As content of the soil sample

Table 1 Physicochemical properties and total and selected extractable contents of Fe, Mn and As in the bulk soil sample

Soil pH and carbon content[a]

pH ($CaCl_2$)	Org. C / g kg^{-1}	Inorg. C / g kg^{-1}
6.6	19.4	<0.2

Total and selected extractable contents of Fe, Mn and As

Element	Total / mg kg^{-1}	Sequential extraction[b] F3	F4	F5	F6
		% of total extracted			
Fe	47 900	—	18	18	64
Mn	600	18	6	8	60
As	41	—	80	9	9

[a]Soil pH and carbon content were determined according to the methods detailed in Dittmar *et al*. (2007) on samples collected at the same site in May 2005.

[b]Only fractions accounting for more than 5% of the total are listed: F3, hydroxylamine ('Mn oxyhydroxides'); F4, acid oxalate ('poorly crystalline Fe oxyhydroxides'); F5, ascorbic acid ('crystalline Fe oxyhydroxides'); F6, residual.

© 2010 The Authors

Table 2 Results of the LCF analysis of the Fe K-edge EXAFS and first-derivative XANES spectra of the bulk soil and representative μ-XAFS spectra (for each spectrum upper row indicates LCF results from the EXAFS region and lower row from the XANES region[a]), Fe(II) fraction derived from LCF, and molar As/Fe ratio

	Bio[b] (%)	CCa-2[b] (%)	IMt-1[c] (%)	SWy-2[c] (%)	Fh[d] (%)	Sum[e] (%)	R^f (%)	Fe(II)[g] (%)	As/Fe[h] (*10^{-3})
Bulk	23	—	30	13	34	105	0.7	24	0.6
	12	—	57	2	29	103	0.5	18	—
High As	14	—	—	13	73	100	2.6	13	15
(outside)[i]	9	—	—	0	91	98	0.7	8	—
High As	—	—	17	—	83	95	5.6	2	4
(inside)[i]	—	—	7	—	93	98	0.8	1	—
Thin[j]	—	—	38	—	62	89	10.2	4	6
	—	—	16	—	84	98	1.3	2	—
Thick[j]	14	—	54	—	33	105	1.3	18	3
	5	—	56	—	39	98	0.8	11	—
Matrix[k]	23	15	23	16	23	111	1.7	38	BKG
	21	7	38	19	16	102	0.8	30	—

[a]The EXAFS spectra were fitted over k-range 3–11 Å^{-1} (except point of interest 'thick': k-range 3–8 Å^{-1}). The first derivative XANES spectra were fitted between 7108 and 7158 eV considering only the references used in the LCF of the corresponding EXAFS spectrum. LCF spectra are shown in Figure 1 (EXAFS) and Figure S2 (first derivative XANES).
[b]Fe(II) phyllosilicates.
[c]Fe(III) phyllosilicates.
[d]Two-line ferrihydrite (as proxy for Fe(III) oxyhydroxides).
[e]Sum of the scaling factors of the single components after fitting; the scaling factors reported for individual species were recalculated to 100%.
[f]R-factor = $\sum(\text{data}_i\text{-fit}_i)^2/\sum\text{data}_i^2$.
[g]Fraction of Fe(II) calculated as the weighted sum of the Fe(II) fractions of the individual reference materials used for LCF (Table S1).
[h]Molar As/Fe ratio; from the quantitative XRF results for the bulk soil and from the (qualitatively) converted μ-XRF intensities ratios for individual POI. At the points of interest 'matrix' no As was detected μ-XRF.
[i]Point of interest on the outside and inside of small root with large As accumulation (Figure 4).
[j]Point of interest in Fe-rich zone around thin (Figure 5) and thick roots (Figure 6).
[k]Typical matrix spectrum away from apparent Fe and As accumulation.

was above average field values at the study site (Dittmar *et al.*, 2007), reflecting the proximity of the sampling location to the irrigation water inlet. Total Fe and Mn contents, on the other hand, were comparable to values determined in the topsoil across the field. About 20% of the total Fe was extracted in both F4 and F5, suggesting that similar fractions of Fe were associated with poorly crystalline and crystalline Fe(III) oxyhydroxides, respectively. The remaining Fe (approximately 60%) was retained in the residual fraction. About 18% of the Mn was extracted in F3 (designed for the reductive release of Mn(III/IV) oxyhydroxides without dissolving Fe(III) oxyhydroxides) and a similar fraction (14%) was released in F4 + F5, suggesting that similar amounts of Mn were contained in pure Mn(III/IV) oxyhydroxides and as trace cations in Fe(III) oxyhydroxides (molar Mn/Fe ratio in F4 and F5 was about 7×10^{-3}). Most As (80%) was oxalate-extractable (F4), suggesting predominant association of As with poorly crystalline Fe(III) oxyhydroxides. Accordingly, the molar As/Fe ratio of oxalate-extractable As and Fe (2.6×10^{-3}) was substantially larger than that of total As and Fe (6×10^{-4}).

Element speciation in bulk soil

To assess the speciation of Fe in the aerated bulk soil after rice harvest we fitted the EXAFS spectrum by a linear combination of a series of reference spectra. Out of the 12 selected reference spectra (Table S1), only 5 were required to reproduce the bulk EXAFS spectrum as well as the μ-EXAFS spectra from selected points-of-interest (POI) on soil thin-sections (Table 2). The respective reference compounds were considered representative proxies for Fe(II) phyllosilicates (Bio, CCa-2), Fe(III) phyllosilicates (IMt-1, SWy-2) and Fe(III) oxyhydroxides (two-line ferrihydrite). Not surprisingly, important contributions of Fe(II) carbonates, Fe(II)-sulphides or aqueous Fe^{2+} (as a proxy for sorbed Fe(II)) were detected in any EXAFS spectrum. Even if the entire reducible sulphate in the soil (approximately 2.2 mmol kg^{-1}) was reduced to sulphide to form FeS, this would have affected <0.5% of the total Fe in the soil. Sorbed Fe(II) that may have formed under predominantly waterlogged conditions at the initial stage of rice growth was probably re-oxidized as the soil underwent a transition towards predominantly oxic conditions towards rice harvest (Roberts, 2009), and any residual adsorbed Fe(II) was probably oxidized during sample treatment. The XANES spectra, the k^3-weighted χ-spectra, and the Fourier transformed EXAFS spectra of these references are included in Figure 1. It is important to note that, given our reference database, the combination of fitted components is most representative for the average bonding environment around Fe in the respective sample rather than best reflecting the exact distribution of species in the soil. (The

© 2010 The Authors

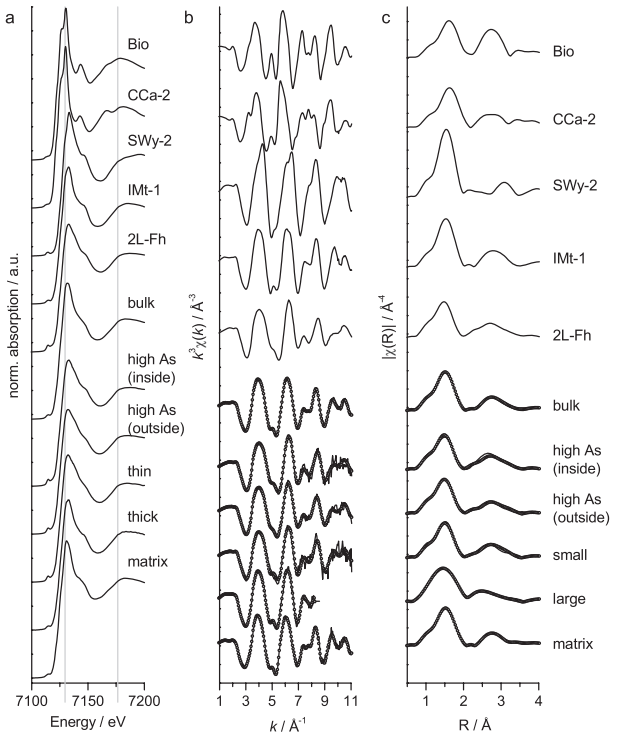

Figure 1 (a) Normalized Fe K-edge XANES, (b) k^3-weighted EXAFS and (c) magnitude of the Fourier transformed EXAFS of the five Fe reference compounds used for LCF (Bio, biotite; CCa-2, chlorite; SWy-2, smectite; IMt-1, illite; 2L-Fh, two-line ferrihydrite), of the bulk soil and of selected POI (labels explained in text). For the sample spectra, the best EXAFS LCF spectra are shown (open dots) in panel b and c; the results are summarized in Table 2. Vertical lines in panel (a) should guide the eye. (First-derivative XANES spectra and corresponding LCF spectra are shown in Figure S2).

bonding environment of Fe in the five reference compounds used is discussed in the Supporting Information.)

Figure 1 shows the normalized bulk Fe K-edge XANES spectrum along with the k^3-weighted χ-spectrum and the Fourier transformed EXAFS spectrum. The best linear combination fit of the bulk averaged EXAFS spectrum required four components, namely biotite, illite, smectite and two-line ferrihydrite. This fit is shown in Figure 1 and the fitted fractions are summarized in Table 2 together with the Fe(II) fraction (as calculated by the weighted sum of the Fe(II) fractions in the individual components Table S2). The fitted fraction of ferrihydrite (34%) is larger than the chemically extracted Fe pool associated with poorly-crystalline Fe hydroxides (F4, 18%) but agrees well with the total pool of Fe oxyhydroxides (F4 + F5, 36%), for which the ferrihydrite reference served as a proxy.

Using the same set of reference compounds, we also determined their relative contributions from a LCF of the XANES spectrum. Because the structural sensitivity differs between XANES and EXAFS, the fitted results are expected to provide complementary information on the average molecular environment of Fe in the sample. The result obtained by fitting the first derivative of the experimental XANES spectrum (Table 1) (Figure S2) differed from the EXAFS LCF results in that the biotite and the smectite fraction diminished each by about 10%, whereas the fitted fraction of illite increased by about 30%. The Fe(II)/Fe_{total} ratios derived from LCF of the EXAFS (24%) and the XANES (18%) spectrum agreed within 6%. As well as determining the Fe(II) fraction from the individual LCF components, we determined the average oxidation state of Fe in the bulk soil by an empirical three-variable method (Marcus *et al*., 2009) and obtained a Fe(II):Fe_{total} ratio of about 20%, which agreed well with the results of the XANES and the EXAFS LCF analysis. Overall, the spectroscopic results thus suggest that about 35% of the Fe in the dried bulk soil was contained in Fe(III) oxyhydroxides, about 20% in Fe(II)-bearing phyllosilicates and about 45% in Fe(III)-bearing phyllosilicates.

The Mn K-edge XANES spectrum of the bulk soil is shown in Figure 2. Manganese may occur in multiple oxidation states even within a single mineral phase. The energy position of the maximum absorbance in the XANES spectrum shifts to greater energy with increasing Mn oxidation state. Although the shape of the absorption edge is influenced by structural and electronic factors, a qualitative evaluation of the occurring Mn oxidation state is possible by fitting the sample spectrum with reference spectra (Guest *et al*., 2002). We selected three references, namely, dissolved Mn^{2+}, ripidolite and Na-birnessite, as proxies for soil Mn(II), Mn(III) and Mn(IV), respectively. However, ripidolite and Na-birnessite also contain in addition some Mn(II) and Mn(III), respectively. The soil XANES spectrum was best fitted with 13% Mn^{2+} (aq), 43% ripidolite and 44% birnessite. The fitted birnessite fraction is larger than the fraction of Mn extracted in F3, which targetted Mn(III/IV) oxyhydroxides (18%, Table 1). The

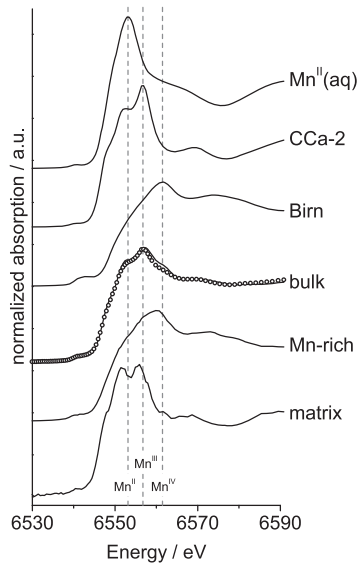

Figure 2 Normalized Mn K-edge XANES spectra of Mn-reference compounds (CCa.2, ripidolite; Birn, Na-birnessite), of the bulk soil, and of representative POI (Mn-rich concretion near thick root (as shown in Figure 6) and soil matrix away from root). The vertical lines indicate the position of the absorption peaks of the reference samples.

© 2010 The Authors

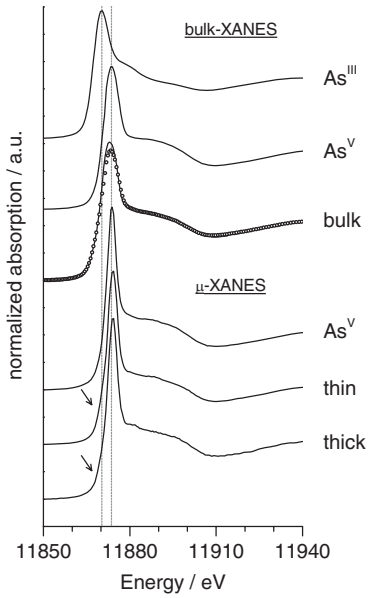

Figure 3 As K-edge XANES spectra of reference samples (As(III) and As(V) sorbed to ferrihydrite) and of the bulk soil. Averaged μ-XANES spectra collected close to a thin root (two points of interest) and close to a thick root (three points of interest) are shown along with the As(V) reference spectrum measured at the same beamline. The arrows point to the slight shoulder in the XANES, indicating a small fraction of As(III).

difference may partly be related to some Mn(III/IV) oxyhydroxides resisting extraction with a mild reductant, as has been shown for a quinol extraction (Guest *et al*., 2002), or to Mn(III) and Mn(IV) incorporated into Fe(III) oxyhydroxides (Scheinost *et al*., 2001), in line with SE results indicating that 14% of the Mn was associated with Fe(III) oxyhydroxides (Table 1). The remaining Mn(III) together with the Mn(II) mainly accounts for Mn bound in the residual fraction, although the small fraction of 13% Mn^{2+} (aq) from the LCF could partly also account for small fractions of exchangeable or specifically bound Mn^{2+} (both estimated as <5% on the basis of SE results).

The normalized As K-edge XANES spectrum of the bulk soil is shown in Figure 3 together with the reference spectra of As(III) and As(V) adsorbed to ferrihydrite, which served as proxies for soil As(III) and As(V) in the LCF. The LCF of the soil As XANES spectrum indicated that about 30% of the total As was As(III), whereas the LCF of the corresponding EXAFS spectrum (k-range, 3–8 $Å^{-1}$) indicated an As(III) fraction of approximately 15% (data not shown). Together with the SE results this suggest that most of the As in the dried bulk soil was As(V) associated with Fe(III) precipitates, but that a minor fraction of adsorbed As(III) persisted in the bulk soil collected after rice harvest.

XRF imaging and typology of concentric element accumulations around roots

Numerous soil thin sections were evaluated by light microscopy. On the basis of the distinct colour of Fe(III) precipitates, diffuse Fe(III) accumulations were observed in the soil matrix as well as marked concentric Fe(III) accumulations (Figure S3). Concentric Fe(III) accumulations around roots were also observed in the field soil profile (Dittmar *et al*., 2007), and the respective features in soil thin-sections were therefore assumed to be related to the presence of O_2-releasing rice roots. Focusing on root-related Fe(III) accumulations, we consequently selected four thin sections for μ-XRF-imaging to determine the distribution of Fe, Mn and As around roots on the micrometre scale (Figures 4–6) for three exemplary regions with concentric Fe(III) accumulations. Additional maps show the μ-XRF-derived molar As/Fe ratio. With respect to the elemental distribution pattern, the concentric element accumulations could be classified according to the following simplified scheme.

Thin roots (diameter < 70 μm) with large As/Fe ratios. We investigated five thin channels with a mean diameter below 70 μm (Figure 4). The roots were in general conserved during the sample preparation and anatomical structures within the root channels were visible. Fe and As are strongly enriched around the cortical region but are also found within the root. Whereas Fe is detected around voids across the whole cross-section, As was not detected in the central part of the root. In the region of largest As accumulation, the As/Fe ratios were largest and exceeded those observed for any other root (*vide infra*) by a factor of about 3–5. Moreover, the maximum Fe and As count rates were much larger for these thin roots than for other categories of roots. Iron and As were enriched up to a distance of only about 50 μm from the root surface. The Mn-rich particle close to the root was identified as a silicate mineral, but no secondary Mn enrichments were observed in the vicinity of the root.

Thin roots (diameter 70–100 μm). Figure 5 shows a thin-section area comprising several thin channels. Intact roots within these channels were in general not visible as they presumably shrunk during sample preparation, but small fragments were visible in some channels. We investigated 20 such thinner channels with a mean diameter varying between 70 and 100 μm. No Mn enrichment was observed around the roots (local Mn-rich spots correspond to Mn-bearing silicates). The Fe count rates were in general largest close to the channel–soil interface and decreased towards the matrix. The As enrichment followed the Fe enrichment closely.

Thick channels (diameter > 200 μm) with Mn and Fe enrichments. The largest concentric enrichment pattern observed was about 2 mm in diameter. Figure 6 shows an example. No roots or root fragments were visible in these channels and were possibly lost during sampling (insertion of the Kubiena box) or had shrunk during sample preparation. The five thick channels examined had a central diameter of 400–500 μm. Whereas Fe was enriched up to a distance of about 1000 μm from the root centre in a nearly concentric manner, discrete secondary Mn enrichments were observed near the root. The Fe count-rates were largest in the region beyond

© 2010 The Authors

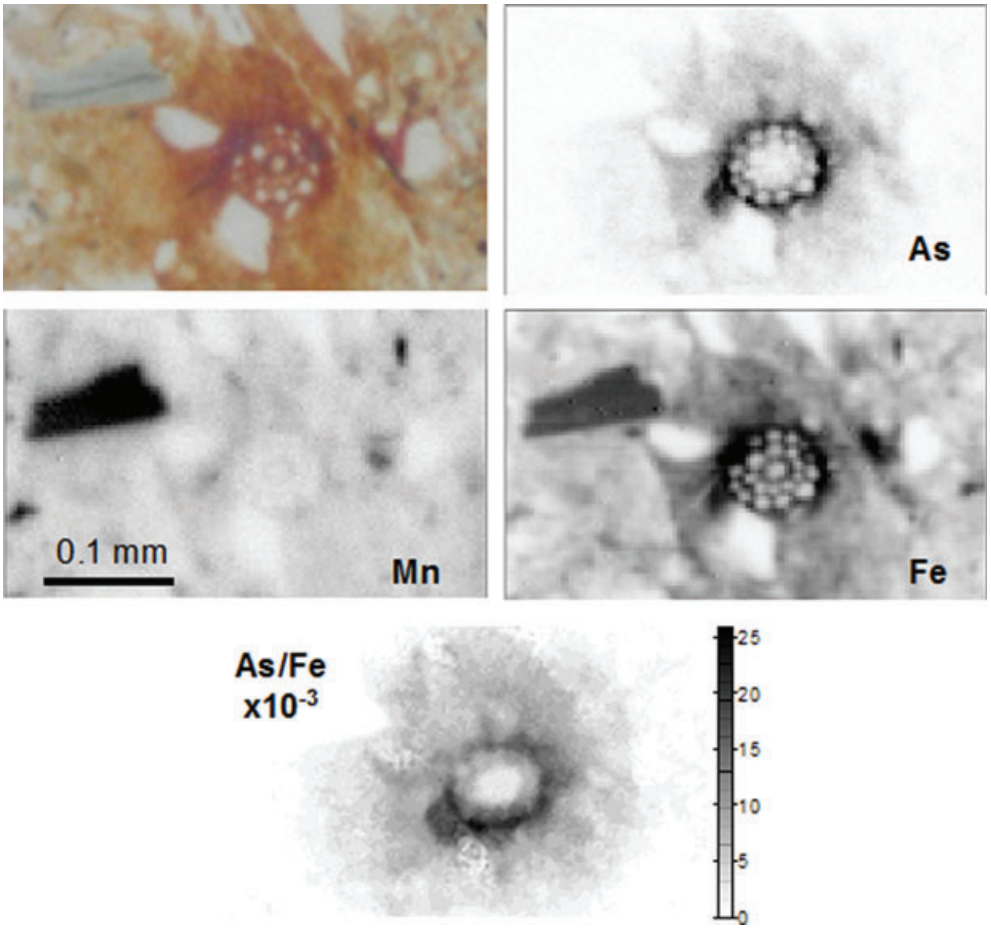

Figure 4 Light microscope image (top left) of a thin root with large As/Fe ratio, along with the distribution of As, Fe and Mn (μ-XRF). As/Fe: calculated molar As/Fe ratio. The Fe μ-XAFS spectra 'high As (inside)' and 'high As (outside)' were collected at several spots within and closely around the thin root. The structure seen inside the root in the Fe and the As maps most probably reflects the internal structure of the plant cortex. The size of the X-ray beam on the sample was 5×5 μm^2 (H × V).

the zone of Mn enrichments. The count rates for Fe in the Fe enrichment zone were smaller than for the thin roots, indicating a lower concentration of accumulated Fe (identical inelastic scattering intensities allowed to exclude pronounced material density variations). The As distribution followed the Fe distribution but the As/Fe ratio increased towards the outer rim of the Fe enrichment zone (Figure 6). The average As/Fe ratio corresponded to that observed for the thin roots (diameter, 70–100 μm). A striking exception to this general pattern was a thick root around which Mn-concretions but no Fe enrichments were detected (Figure S4).

Micro-XAFS spectroscopy

μ-XANES (for Fe, Mn and As) and μ-EXAFS (for Fe) spectra were collected on selected points of interest, which were either located in the soil matrix and away from roots or could be assigned to element accumulations around one of the root types defined above. The Fe spectra (Figure 1) were evaluated quantitatively by LCF using the same components as for the bulk analysis (Table 2). Representative spectra for Fe around a thin root with a diameter below 70 μm (Figure 4) with strong As enrichment and for Fe in the region inside the same thin root are shown in Figure 1 and are referred to as 'high As (outside)' and 'high As (inside)', respectively. Both spectra resemble most closely the two-line ferrihydrite reference spectrum, suggesting that a ferrihydrite-like Fe(III) oxyhydroxide is the dominating Fe species within and around the thin roots. The ferrihydrite fraction fitted for the Fe-EXAFS collected around a thin root with a smaller As/Fe intensity-ratio, comparable to those shown in Figure 5, was slightly smaller (Table 2). In the Fe-rich region around thick roots (Figure 6), ferrihydrite was still enriched (Table 2) compared with the bulk and matrix spectrum but to a lesser extent than in the Fe(III) accumulations around thin roots (Table 2). Finally, the LCF of an exemplary matrix spectrum shows that the Fe speciation in the matrix was dominated by Fe(II)- and Fe(III)-bearing phyllosilicates. Together, these findings show that Fe was enriched around the roots mainly as ferrihydrite-like Fe(III)

© 2010 The Authors

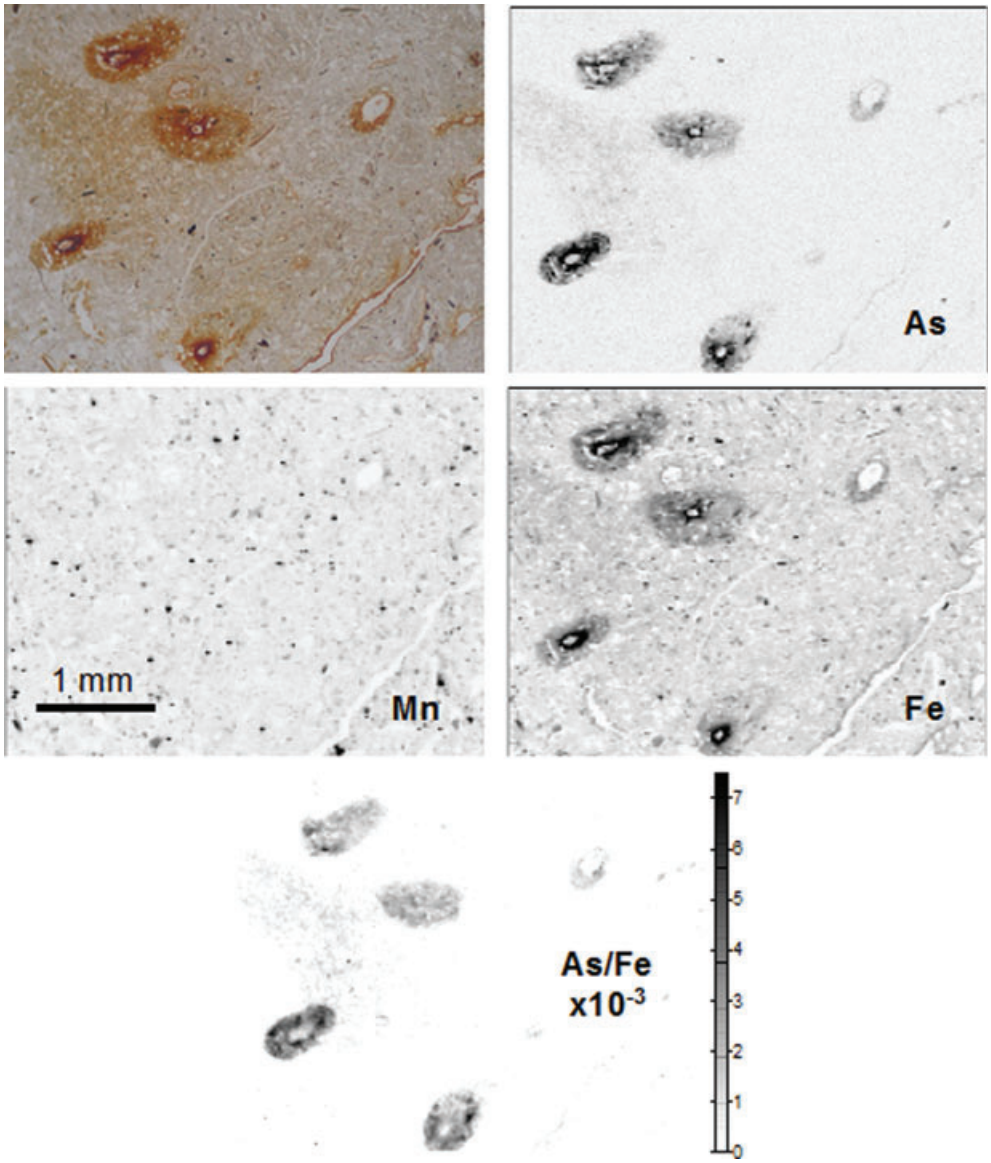

Figure 5 Light microscope image (top left) of a region containing thin roots, along with the distribution of As, Fe and Mn (μ-XRF). As/Fe: calculated molar As/Fe ratio. The size of the X-ray beam on the sample was 16 × 7 μm^2 (H × V).

precipitates, in line with results of previous spectroscopic studies (Hansel *et al*., 2002; Voegelin *et al*., 2007).

An exemplary Mn μ-XANES spectrum for a Mn-enrichment close to the surface of a thick root (Figure 6) is shown in Figure 2. The spectrum resembles the birnessite reference spectrum, thus suggesting that Mn(III/IV) oxides were the dominant species. The Mn μ-XANES collected in the soil matrix was characterized by an intense split whiteline at lower energies, indicative of the presence of Mn(II) and Mn(III) in phyllosilicates.

Arsenic μ-XANES spectra with good signal-to-noise ratios were only collected from enrichments around the roots, but not in the soil matrix. Two averaged μ-XANES spectra collected in the Fe(III) enrichments around a thin root with a large As/Fe ratio (two spectra, Figure 4) and around a thick root (three spectra, Figure 6) are shown in Figure 3. Both spectra are similar to the As(V) reference, indicating that accumulated As in the rhizosphere was mainly As(V). However, the slight shoulders at the low-energy side of the absorption edge (arrows in Figure 3) indicate a small fraction of As(III).

Discussion

Fe and Mn enrichment patterns and their relation to the rice root system

The μ-XRF element mapping revealed two dominant and distinct types of Fe and Mn enrichment patterns around roots:

© 2010 The Authors

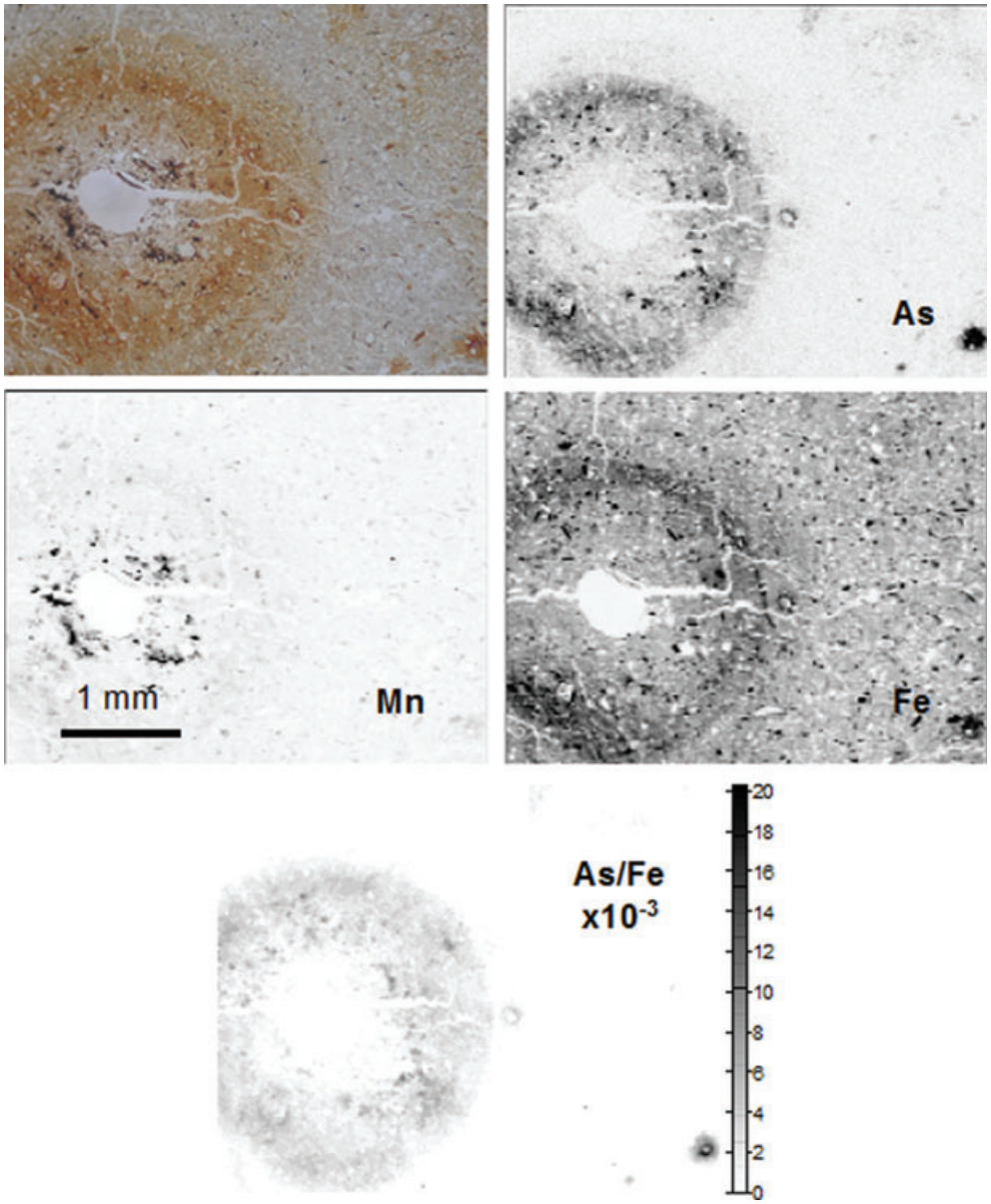

Figure 6 Light microscope image (top left) of a region containing a thick root and a thin root with large As/Fe ratio (shown in detail in Figure 4), along with the distribution of As, Fe and Mn (μ-XRF). As/Fe: calculated molar As/Fe ratio. The size of the X-ray beam on the sample was 16 × 7 μm^2 (H × V).

(i) concentric Fe(III) accumulations in the rhizosphere soil away from the root surface combined with discrete Mn enrichments close to the root–soil interface around thick roots (diameters of around 500 μm) and (ii) large Fe concentrations directly at the root–soil interface but no detectable Mn accumulation around thin roots (diameters < 100 μm). These patterns closely match the subdivision of rice roots into primary and lateral roots with typical diameters of 1 and 0.1 mm, respectively. The aerenchyma of primary roots ensures the transport of O_2 to distant parts of the root (Kirk, 2004). Because primary roots develop gas-impermeable layers towards the shoot (Kirk, 2003), radial O_2 loss is largest from the first few centimetres from the root tip (apex) (Armstrong *et al*., 2000). Lateral roots branch from the primary roots and grow to a length of 1–2 cm (Kirk, 2004). Their walls are gas-permeable to maintain their ability to absorb nutrients and thus leak O_2 into the soil (Armstrong *et al*., 2000). Microsensor studies have shown that an oxygenated zone develops around submerged primary roots, extending several hundreds of micrometres inside the anoxic matrix (Flessa & Fischer, 1992; Revsbech *et al*., 1999; Armstrong *et al*., 2000). Although direct loss of O_2 from primary roots may be small, large numbers of emerging laterals with overlapping rhizospheres may maintain a concentric oxidized zone around primary roots (Colmer, 2003). In contrast, the O_2-enriched zone around a single lateral root

© 2010 The Authors

is confined to a significantly smaller volume (radius of around 100 μm) and maximum O_2 saturation levels are about one order of magnitude smaller (Revsbech *et al*., 1999).

The diameter and shape of the intercellular space identify the thin roots (Figure 4) as lateral roots or apical primary roots. The Fe distribution pattern clearly shows Fe enrichments within the roots. Fe precipitates have been observed along cell walls and within intercellular spaces of rice roots (Green & Etherington, 1977; Chen *et al*., 1980). Moreover, similar Fe enrichments were reported from cross-sectional X-ray tomography images of roots of an aquatic plant (*Phalaris arundinacea*) (Hansel *et al*., 2002). The formation of Fe precipitates inside the root is thought to follow cell walls as a template and to occur mainly in dead, outer cells (Green & Etherington, 1977; Chen *et al*., 1980). Both outside and inside the roots, LCF analysis indicated that Fe was mainly present as ferrihydrite-like precipitate, in line with the marked Fe accumulation relative to the soil matrix. The diameter of the central channel visible in Figure 6 fits well with literature values for the diameter of primary roots and the maximum extension of the Fe enrichment zone agrees with the dimensions of the oxidized zone around primary roots (Revsbech *et al*., 1999). LCF analysis of the Fe μ-EXAFS spectrum collected in the vicinity of the thick root indicated that about 35% of the Fe was in Fe(III) oxyhydroxides, reflecting only moderate Fe accumulation relative to the matrix soil (Table 2).

Mechanisms responsible for distinct Fe and Mn enrichment patterns

The redistribution of Fe and Mn in submerged soils results from their reductive mobilization in the anoxic matrix, the subsequent diffusive or advective transport towards (partly) oxidized zones, and the oxidative immobilization through precipitation of sparingly soluble phases. Concentric Fe accumulations in the rhizosphere of wetland plants are well documented (Green & Etherington, 1977; Voegelin *et al*., 2007). Their formation has been attributed to the Liesegang phenomenon (Saleque & Kirk, 1995) arising from the coupling of diffusion and chemical reactions (Kirk, 2004). The formation of concentric Fe enrichments around rice roots has been shown by model calculations to result from the coupled movement of O_2, Fe^{2+}, and acidity between the reduced soil matrix and the O_2-releasing root surface and the pH-dependence of Fe^{2+} sorption and mobility (Kirk *et al*., 1990). Sensitivity analysis further indicated that the position and extent of Fe enrichments depends on a variety of factors, including soil texture, Fe content, pH buffering capacity, release rate of O_2 from roots and time over which Fe accumulation forms. Furthermore, the varying degree of soil flooding (Roberts, 2009) and changes in the spatial pattern of O_2 losses within the root system will affect the element enrichments observed in the rhizosphere after the growth period.

The diffusive and advective transport of Mn^{2+} and Fe^{2+} in soil can be assumed to be similar. However, Mn and Fe differ distinctly in their redox behaviour. Already at moderately reducing conditions, Mn(III/IV) oxyhydroxides are reductively dissolved, whereas more strongly reducing conditions are required to reduce Fe(III) phases. Conversely, the oxidation of Fe^{2+} proceeds at smaller redox potentials than the oxidation of Mn^{2+}. The abiotic oxidation of Fe^{2+} by O_2 proceeds rapidly at atmospheric pO_2 and near neutral pH, but microbial Fe^{2+} oxidation with O_2 may dominate in micro-aerophilic environments (Neubauer *et al*., 2007). In contrast, the homogeneous oxidation of Mn^{2+} by O_2 is extremely slow (Morgan, 2005). Also surface-catalyzed oxidation rates of Mn^{2+} at near-neutral pH are typically smaller than rates reported for microbial Mn^{2+} oxidation (Bargar *et al*., 2009). Mn(III/IV) oxyhydroxides formed in natural systems are therefore assumed to be mostly of biogenic origin, although they may be further transformed abiotically (Bargar *et al*., 2009).

Around the thick roots (Figure 6), the observed spatial pattern of Mn(III/IV) oxyhydroxides close to the root surface followed by concentric Fe(III) oxyhydroxide precipitates away from the root surface is thus in line with the expected sequence, mechanisms and kinetics of oxidation reactions as a function of the redox potential, which is greatest close to the root–soil interface (Revsbech *et al*., 1999). The single observation of a thick root with significant accumulation of Mn(III/IV) oxyhydroxides at the root surface but minor Fe accumulation (Figure S4) points to the importance of the temporal coincidence between root growth, rate of O_2 release and soil redox dynamics. Exclusive accumulation of Mn around thicker roots could for instance be expected at later stages of rice growth where irrigation is less intense and the soil experiences prolonged periods over which Mn but not Fe is reductively mobilized from the soil matrix (Roberts, 2009) and accumulated by oxidation near roots.

In contrast to thick roots, Fe(III) oxyhydroxides accumulated directly at the surface of thin roots and Mn(III/IV) oxyhydroxides did not form (Figures 4 and 5). These two differences between thick and thin roots imply that the redox at the surface of thin roots did not reach potentials sufficiently large for Mn^{2+} oxidation over an extended period. The smaller redox potentials can be either related to a smaller O_2 flux at the channel-soil interface or to a dilution effect. Neglecting O_2 consumption, this can be qualitatively rationalized by mass conservation, which requires that the O_2 flux originating from a curved root surface decreases by 50% over a distance equivalent to the root diameter. Thus, around thicker roots, larger redox potentials can be maintained over longer distances. Around thin roots, on the other hand, the decrease of the O_2 flux with distance from the root surface may be too strong to meet the conditions for Mn^{2+} oxidation, and Fe^{2+} oxidation and precipitation occur immediately at the root surface. Including O_2 consumption from redox reactions will complicate the situation, but will not affect the general conclusion from our qualitative consideration.

Consequences for As dynamics in the rhizosphere soil

The μ-XRF results showed a strong variation in the As distribution within the sample and a close correlation between As and Fe

© 2010 The Authors

enrichments as well as an anti-correlation between As and Mn enrichments. This observation is in agreement with previous micro-spectroscopic studies on the distribution of Fe, Mn and As around the roots of perennial plants in a contaminated floodplain soil (Voegelin *et al*., 2007) and in a marine ferromanganese nodule (Marcus *et al*., 2004). During periodic irrigation and submergence of the paddy soil, the reductive mobilization of Mn occurs at a higher redox potential than the reduction of Fe(III) and As(V) (Masscheleyn *et al*., 1991). With further decreasing redox potential, As is mobilized because of the combined effects of reductive dissolution of Fe(III) oxyhydroxides (that act as sorbents for As) and the reduction of As(V) to the less strongly adsorbing As(III) (Weber *et al*., 2010). Thus, the mobilization of As parallels the mobilization of Fe, as reflected in the temporal and spatial correlation of As and Fe in the pore water at the site (Roberts, 2009). Advective and diffusive processes lead to a transport of the dissolved Fe and As to the oxidation zone around the channels. The oxidation of Fe and the formation of Fe(III) precipitates generally entail the immobilization of As, as the oxidation of Fe^{2+} catalyzes the oxidation of As(III) (Roberts *et al*., 2004), and as both As(III) and As(V) sorb to, or co-precipitate with, Fe(III) precipitates (Voegelin *et al*., 2007, 2010). The co-oxidation of As(III) with Fe(II) proceeds at redox potentials at which Mn(II) oxidation does not yet occur, explaining the selective association of As with Fe, but not Mn, enrichments. The As K-edge XANES spectra (Figure 3) show that, at the end of the growth period, the As is mainly present as As(V). Thus, the processes responsible for the two distinct Fe enrichment patterns also shape the distribution of As. This strong link between the Fe and As dynamics is supported by the SE results, suggesting that the majority of the As is associated with Fe(III) oxyhydroxides. The molar As/Fe ratios determined by μ-XRF around the roots lie within the range (1×10^{-3} to 0.1) of literature values obtained by chemically dissolving the Fe plaque adhering to roots (Blute *et al*., 2004; Hossain *et al*., 2009). The measured molar As/Fe ratios are larger for the thin roots than for the thick roots (Table 2; Figures 4–6). This probably reflects the greater enrichment of Fe (and As) around thin roots than around thick roots: thus a larger percentage of the Fe around large roots is associated with primary minerals and causes the molar ratio of total As/Fe to be smaller than the ratio of enriched As/Fe. Notably, the largest As/Fe ratio, found for the thin As-rich roots (Table 2), is about a factor of 10 larger than the As/Fe ratio of the oxalate extract (F4, Table 1). This difference clearly indicates that the As-loading of short-range-ordered Fe(III) precipitates varies within the soil sample, which may have implications for the uptake of As by rice and the dynamics of As release under reducing conditions.

Conclusions

To study the As retention in the rhizosphere of wetland plants, roots are often removed from the soil and only the plaque adhering to the root surface is analysed. This surface plaque has a typical thickness of a few tens of microns (Blute *et al*., 2004). Our results demonstrate that rice roots influence soil Fe, Mn and As distribution up to 1 mm away from the root–soil interface. The element-distribution pattern and the molar As/Fe ratio show a pronounced spatial variability and differ distinctly around lateral and primary roots. Banded accumulation of Fe away from the root-soil interface may for example explain the absence of visual evidence for the formation of Fe plaque around a washed rice root grown under submerged conditions (Smith *et al*., 2009). Thus, our results indicate that in addition to the Fe plaque adhering to the roots, Fe(III) precipitates in the surrounding rhizosphere soil and related As retention mechanisms must be considered to obtain a better understanding of the processes controlling the transfer of As into rice. Both phosphate and silicate strongly influence the type of Fe(III) precipitate forming and the extent of As sorption (Roberts *et al*., 2004; Voegelin *et al*., 2010) and also interfere with As uptake by rice (Li *et al*., 2009; Zhao *et al*., 2009). Therefore, these oxyanions should be included in future studies on coupled As and Fe dynamics in the rhizosphere soil and their implications for As uptake by rice.

Supporting Information

The following supporting information is available in the online version of this article:

S1. Further details on the bulk and micro XAFS and XRF analysis.

S2. Discussion of the Fe reference compounds.

S3. XRD analysis of the topsoil sample.

S4. Fe K-edge XANES LCF.

S5. Additional figures.

Please note: Blackwell Publishing is not responsible for the content or functionality of any supplementary materials supplied by the authors. Any queries (other than missing material) should be directed to the corresponding author for the article.

Acknowledgements

We thank Kurt Barmettler for technical support and Marc Herrmann for performing the sequential extraction. Mirjam Kiczka, Jan Wiederhold, Olivier Jacquat and Peter Brack are acknowledged for providing reference phases. We acknowledge the HASYLAB, the ANKA, the ESRF and the ALS for provision of synchrotron radiation facilities. Edmund Welter (HASYLAB), Sirine Fakra (ALS), Herman Emerich, Wouter van Beek (both ESRF) and Stefan Mangold (ANKA) are thanked for their assistance during data collection. The ALS is supported by the Director, Office of Science, Office of Basic Energy Sciences, Materials Sciences Division, of the US Department of Energy under Contract No DE-AC03-76SF00098 at Lawrence Berkeley National Laboratory. Part of this work was funded by the Swiss National Science Foundation through grants No 200021-105612 and 200020-113654.

© 2010 The Authors

References

Armstrong, W. 1971. Radial oxygen losses from intact rice roots as affected by distance from apex respiration and waterlogging. *Physiologia Plantarum*, **25**, 192–197.

Armstrong, W., Cousins, D., Armstrong, J., Turner, D.W. & Beckett, P.M. 2000. Oxygen distribution in wetland plant roots and permeability barriers to gas-exchange with the rhizosphere: a microelectrode and modelling study with *Phragmites australis*. *Annals of Botany*, **86**, 687–703.

Bargar, J.R., Fuller, C.C., Marcus, M.A., Brearley, A.J., Perez De la Rosa, M., Webb, S.M. *et al*. 2009. Structural characterization of terrestrial microbial Mn oxides from Pinal Creek, AZ. *Geochimica et Cosmochimica Acta*, **73**, 889–910.

Blute, N.K., Brabander, D.J., Hemond, H.F., Sutton, S.R., Newville, M.G. & Rivers, M.L. 2004. Arsenic sequestration by ferric iron plaque on cattail roots. *Environmental Science & Technology*, **38**, 6074–6077.

Caetano, M. & Vale, C. 2000. Retention of arsenic and phosphorus in iron-rich concretions of Tagus salt marshes. *Marine Chemistry*, **79**, 261–271.

Chen, C.C., Dixon, J.B. & Turner, F.T. 1980. Iron coatings on rice roots: morphology and models of development. *Soil Science Society of America Journal*, **44**, 1113–1119.

Colmer, T.D. 2003. Long-distance transport of gases in plants: a perspective on internal aeration and radial oxygen loss from roots. *Plant, Cell & Environment*, **26**, 17–36.

Dittmar, J., Voegelin, A., Roberts, L.C., Hug, S.J., Saha, G.C., Ali, M.A. *et al*. 2007. Spatial distribution and temporal variability of arsenic in irrigated rice fields in Bangladesh. 2. Paddy soil. *Environmental Science & Technology*, **41**, 5967–5972.

Fitz, W.J. & Wenzel, W.W. 2002. Arsenic transformations in the soil-rhizosphere-plant system: fundamentals and potential application to phytoremediation. *Journal of Biotechnology*, **99**, 259–278.

Flessa, H. & Fischer, W.R. 1992. Plant-induced changes in the redox potentials of rice rhizospheres. *Plant & Soil*, **143**, 55–60.

Green, M.S. & Etherington, J.R. 1977. Oxidation of ferrous iron by rice (*Oryza sativa L.*) roots: mechanism for waterlogging tolerance? *Journal of Experimental Botany*, **28**, 678–690.

Guest, C.A., Schulze, D.G., Thompson, I.A. & Huber, D.M. 2002. Correlating manganese X-ray absorption near-edge structure spectra with extractable soil manganese. *Soil Science Society of America Journal*, **66**, 1172–1181.

Hansel, C.M., La Force, M.J., Fendorf, S. & Sutton, S. 2002. Spatial and temporal association of As and Fe species on aquatic plant roots. *Environmental Science & Technology*, **36**, 1988–1994.

Hossain, M.B., Jahiruddin, M., Loeppert, R.H., Panaullah, G.M., Islam, M.R. & Duxbury, J.M. 2009. The effects of iron plaque and phosphorus on yield and arsenic accumulation in rice. *Plant & Soil*, **317**, 167–176.

Kirk, G.J.D. 2003. Rice root properties for internal aeration and efficient nutrient acquisition in submerged soil. *New Phytologist*, **159**, 185–194.

Kirk, G.J.D. 2004. *The Biogeochemistry of Submerged Soils.* Wiley, Chichester, UK.

Kirk, G.J.D., Ahmad, A.R. & Nye, P.H. 1990. Coupled diffusion and oxidation of ferrous iron in soils. II. A model of the diffusion and reaction of O_2, Fe^{2+}, H^+ and HCO_3^- in soils and a sensitivity analysis of the model. *Journal of Soil Science*, **41**, 411–431.

Li, R.Y., Stroud, J.L., Ma, J.F., McGrath, S.P. & Zhao, F.J. 2009. Mitigation of arsenic accumulation in rice with water management and silicon fertilization. *Environmental Science & Technology*, **43**, 3778–3783.

Liu, W.J., Zhu, Y.G., Smith, F.A. & Smith, S.E. 2004. Do phosphorus nutrition and iron plaque alter arsenate (As) uptake by rice seedlings in hydroponic culture? *New Phytologist*, **162**, 481–488.

Liu, W.J., Zhu, Y.G., Hu, Y., Williams, P.N., Gault, A.G., Meharg, A.A. *et al*. 2006. Arsenic sequestration in iron plaque, its accumulation and speciation in mature rice plants (*Oryza sativa* L.). *Environmental Science & Technology*, **40**, 5730–5736.

Marcus, M.A., Manceau, A. & Kersten, M. 2004. Mn, Fe, Zn, and As speciation in a fast-growing ferromanganese marine nodule. *Geochimica et Cosmochimica Acta*, **68**, 3125–3136.

Marcus, M.A., Westphal, A.J. & Fakra, S.C. 2009. Classification of Fe-bearing species from K-edge XANES data using two-parameter correlation plots (vol 15, pg 463, 2008). *Journal of Synchrotron Radiation*, **16**, 439–439.

Masscheleyn, P.H., Delaune, R.D. & Patrick, W.H. 1991. Effect of redox potential and pH on arsenic speciation and solubility in a contaminated soil. *Environmental Science & Technology*, **25**, 1414–1419.

Morgan, J.J. 2005. Kinetics of reaction between O_2 and Mn(II) species in aqueous solutions. *Geochimica et Cosmochimica Acta*, **69**, 35–48.

Neubauer, S.C., Toledo-Durán, G.E., Emerson, D. & Megonigal, J.P. 2007. Returning to their roots: iron-oxidizing bacteria enhance short-term plaque formation in the wetland-plant rhizosphere. *Geomicrobiology Journal*, **24**, 65–73.

Otte, M.L., Kearns, C.C. & Doyle, M.O. 1995. Accumulation of arsenic and zinc in the rhizosphere of wetland plants. *Bulletin of Environmental Contamination & Toxicology*, **55**, 154–161.

Panaullah, G.M., Alam, T., Hossain, M.B., Loeppert, R.H., Lauren, J.G., Meisner, C.A. *et al*. 2009. Arsenic toxicity to rice (*Oryza sativa* L.) in Bangladesh. *Plant & Soil*, **317**, 31–39.

Ravel, B. & Newville, M. 2005. ATHENA, ARTEMIS, HEPHAESTUS: data analysis for X-ray absorption spectroscopy using IFEFFIT. *Journal of Synchrotron Radiation*, **12**, 537–541.

Revsbech, N.P., Pedersen, O., Reichardt, W. & Briones, A. 1999. Microsensor analysis of oxygen and pH in the rice rhizosphere under field and laboratory conditions. *Biology & Fertility of Soils*, **29**, 379–385.

Roberts, L.C. 2009. *Arsenic Dynamics in Groundwater-Irrigated and Seasonally Flooded Paddy Soils in Bangladesh*. Dissertation No 18553, ETH Zurich, Switzerland.

Roberts, L.C., Hug, S.J., Ruettimann, T., Billah, M., Khan, A.W. & Rahman, M.T. 2004. Arsenic removal with iron(II) and iron(III) waters with high silicate and phosphate concentrations. *Environmental Science & Technology*, **38**, 307–315.

Roberts, L.C., Hug, S.J., Dittmar, J., Voegelin, A., Saha, G.C., Ali, M.A. *et al*. 2007. Spatial distribution and temporal variability of arsenic in irrigated rice fields in Bangladesh. 1. Irrigation water. *Environmental Science & Technology*, **41**, 5960–5966.

Roberts, L.C., Hug, S.J., Dittmar, J., Voegelin, A., Kretzschmar, R., Wehrli, B. *et al*. 2009. Arsenic release from paddy soils during monsoon flooding. *Nature Geoscience*, **3**, 53–59.

Saleque, M.A. & Kirk, G.J.D. 1995. Root-induced solubilization of phosphate in the rhizosphere of lowland rice. *New Phytologist*, **129**, 325–336.

Scheinost, A.C., Stanjek, H., Schulze, D.G., Gasser, U. & Sparks, D.L. 2001. Structural environment and oxidation state of Mn in goethite-groutite solid-solutions. *American Mineralogist*, **86**, 139–146.

Smith, E., Kempson, I., Juhasz, A.L., Weber, J., Skinner, W.M. & Gräfe, M. 2009. Localization and speciation of arsenic and trace elements in rice tissues. *Chemosphere*, **76**, 529–535.

© 2010 The Authors

Voegelin, A., Weber, F.-A. & Kretzschmar, R. 2007. Distribution and speciation of arsenic around roots in a contaminated riparian floodplain soil: micro-XRF element mapping and EXAFS spectroscopy. *Geochimica et Cosmochimica Acta*, **71**, 5804–5820.

Voegelin, A., Kaegi, R., Frommer, J., Vantelon, D. & Hug, S.J. 2010. Effect of phosphate, silicate, and Ca on Fe(III)-precipitates formed in aerated Fe(II)- and As(III)-containing water studied by X-ray absorption spectroscopy. *Geochimica et Cosmochimica Acta*, **74**, 164–186.

Weber, F.-A., Hofacker, A., Voegelin, A. & Kretzschmar, R. 2010. Temperature dependence and coupling of iron and arsenic reduction and release during flooding of a contaminated soil. *Environmental Science & Technology*, **44**, 116–122.

Xu, X.Y., McGrath, S.P., Meharg, A.A. & Zhao, F.J. 2008. Growing rice aerobically markedly decreases arsenic accumulation. *Environmental Science & Technology*, **42**, 5574–5579.

Zeien, H. & Brümmer, G.W. 1989. Chemische Extraktion zur Bestimmung von Schwermetallbindungsformen in Böden. *Mitteilungen der Deutschen Bodenkundlichen Gesellschaft*, **59**, 505–510.

Zhao, F.J., Ma, J.F., Meharg, A.A. & McGrath, S.P. 2009. Arsenic uptake and metabolism in plants. *New Phytologist*, **181**, 777–794.

© 2010 The Authors
Journal compilation © 2010 British Society of Soil Science,

Biogeochemical processes and arsenic enrichment around rice roots in paddy soil: Results from micro-focused X-ray spectroscopy

J. FROMMER [a], A. VOEGELIN[b], J. DITTMAR [a], M. A. MARCUS[c], R. KRETZSCHMAR [a]

[a]*Soil Chemistry Group, Institute of Biogeochemistry and Pollutant Dynamics, ETH Zurich, CHN, CH-8092 Zurich, Switzerland.*

[b]*Eawag, Swiss Federal Institute of Aquatic Science and Technology, Ueberlandstrasse 133, CH-8600 Duebendorf, Switzerland*

[c]*Advanced Light Source, Lawrence Berkeley National Laboratory, MS 6-2100, Berkeley, CA 94720, USA,*

Correspondence: A. Voegelin. E-mail: andreas.voegelin@eawag.ch .

Supporting Information

(11 pages, 1 table, 4 figures)

S1 XAS and XRF analysis 2

S2 Iron reference compounds 5

S3 X-ray diffraction analysis of the topsoil sample 7

S4 Fe K-edge XANES LCF 8

S5 Additional figures 10

Literature cited 11

S1 XAS and XRF analysis

XAS data evaluation

For the Fe data, we fixed E_0 to 7128 eV, subtracted a linear pre-edge function fitted between 7028 and 7098 eV, and normalized the data to unit edge jump by extrapolating a second-order polynomial fitted between 7178 and 7698 eV to E_0.

For the Mn data we fixed E_0 to 6550 eV, subtracted a linear pre-edge function fitted between 6450 and 6520 eV, and normalized the data to unit edge jump by extrapolating a first-order polynomial fitted between 6600 and 6830 eV to E_0. The normalized XANES spectrum of the bulk soil was analyzed by LCF using reference spectra of dissolved Mn^{2+} (50 mM $MnCl_2$), ripidolite (natural specimen, source clay CCa-2, containing mainly Mn(III)), and Na-birnessite (synthesized as described elsewhere (Jacquat *et al.*, 2008), but without addition of Zn) as fit components (energy range of the fit: 6535-6580 eV).

For the As data we fixed E_0 to 11871 eV, subtracted a linear pre-edge function fitted between 11771 and 11856 eV, and normalized the data to unit edge jump by extrapolating a first-order polynomial fitted between 11971 and 12171 eV to E_0. The average As oxidation state in the soil sample was determined by LCF of the normalized XANES using the normalized XANES spectra of As(III) and As(V) adsorbed to ferrihydrite (Voegelin *et al.*, 2007) (energy range: 11851-11901 eV) and by LCF of the EXAFS spectrum using the same references (*k*-range: 3-8 $Å^{-1}$).

Micro-focused X-ray analysis

To reduce beam-induced speciation changes, the soil sections were mounted on a Peltier cooling stage (surface temperature: ~27°C; dry N_2 atmosphere to prevent ice formation) in a 45° angle to the incident beam, and the fluorescence signal was recorded in a 90° angle using a Ge 7-element solid state detector. Distribution maps for As and Fe were collected with an incident photon energy

of 13 keV. Maps for Mn were measured with an incident photon energy of 7 keV to prevent leakage of Fe K_α fluorescence into the Mn channel. Evaluation of the μ-XRF mapping-data was done by software developed at ALS beamline 10.3.2. For all element maps shown, the black-level was set to 0 counts and the white-level to the 98th percentile (i.e., 98% of the pixels have an intensity smaller or equal to the white-level). Furthermore, we calculated distribution maps for the XRF-derived molar As/Fe ratios. Before calculating the ratio of the respective XRF channels, we subtracted a background level (resulting from scattering and sample fluorescence other than As K_α-fluorescence) from the As channel counts. This background level was determined by averaging the count-rate in the As channel at several spots in the soil matrix (i.e., away from roots) for which the full XRF spectrum indicated the absence of As K_α fluorescence. To convert this intensity ratio into a molar ratio, we determined a conversion factor as described in the next paragraph.

The sections are polished to a thickness of about 30 μm. Considering the 45° angle of incidence of incoming and outgoing X-rays this sample thickness corresponds to a maximum pathlength of 42 μm (one-way) in the sample. Assuming an average bulk soil density of 1 g cm^{-3} (Dittmar *et al.*, 2007) and using the average elemental composition of the topsoil matrix as determined by bulk XRF analysis, we calculate an absorption length of 110 μm and 750 μm for photon-energies of 5.9 keV (Mn K_α-fluorescence) and 13 keV (excitation energy used for XRF imaging), respectively (cross-sections from Elam database). The path-lengths in the sample are thus well below the absorption length of the relevant excitation and fluorescence energies and we conclude that the thin-layer approximation can be applied. To calculate the (matrix independent) factor for the conversion of Fe/As XRF-intensity ratios into Fe/As mass ratios, we determined the sensitivities (I_0 normalized photon count rate per mass density) of these two elements on foil standards (MICROMATTER™, Vancouver, Canada), with a thin film of Fe (43.9 ± 2.2 μg Fe cm^{-2}) and GaAs (47.8 ± 2.4 μg GaAs cm^{-2}), respectively, deposited onto a Mylar backing. The mass fraction of As in the latter standard was calculated from the fluorescence intensities by using the

tabulated absorption cross-section and the fluorescence yields (Krause, 1979; Elam *et al.*, 2002). The same sample-detector geometry and the same sample-detector distance than for the analysis of the sample sections were used. The calculated sensitivity ratio (sensitivity(As)/sensitivity(Fe)) was 2.57. Thus, experimental As/Fe intensity-ratios can be converted into As/Fe mass-ratios and mole-ratios by a multiplication with a factor of 0.39 and 0.29, respectively.

At selected points of interest (POI), μ-XANES (Fe, Mn, and As) and μ-EXAFS (Fe) spectra were recorded. In general, multiple scans were collected from the same spot. Sporadically, consecutive scans revealed beam-induced reduction of Fe, Mn, and As. In this case, only the first scan was used for further analysis. For As K-edge XAFS, an Al-foil was occasionally placed in front of the detector to mitigate background fluorescence. The Si(111) DCM was calibrated with Fe- and Mn-foil spectra which were aligned to the respective reference spectra of the bulk beamlines. In the case of the As K-edge XAFS spectra, the calibration was done by setting the maximum in the absorption spectrum (whiteline) of As(V) adsorbed to ferrihydrite to 11873.7 eV.

S2 Iron reference compounds

The full set of Fe reference compounds used is listed in Table S1; a subset including only 5 reference compounds was needed to reproduce the experimental spectra. The Fe speciation in the reference compounds of this subset are discussed below:

The two selected Fe(II) containing phyllosilicates, biotite and the source clay reference chlorite CCa-2, are both trioctahedral minerals. The biotite sample contained about 3 wt% Mg and 16 wt% Fe, 87% of which occurs in the form of Fe(II) (Table S1). The next nearest metals around Fe in the octahedral sheet are predominantly Fe atoms as indicated by the intense second shell in the Fourier transformed spectrum (Figure 1c). A quantitative analysis of the Fe K pre-edge XANES spectrum of CCa-2 indicated that 91% of the Fe is present as Fe(II), which agrees well with the Fe(II) fraction (90%) determined in a Mössbauer spectroscopic study of the related reference clay CCa-1 (Drodt *et al.*, 1997). The weaker second shell peak in the Fourier transform and the higher Mg content (6.5 wt%) indicate that the number of next nearest iron neighbors is smaller for CCa-2 than for the biotite reference.

The two Fe(III) containing phyllosilicates, the source clay reference illite IMt-1 and smectite SWy-2, are both dioctahedral minerals. They differ in the total Fe content (IMt-1: 5 wt% Fe, SWy-2: 3 wt% Fe) and in the number of next-nearest-iron neighbors: while on the average 1 out of 4 octahedral metals/metalloids in IMt-1 is an Fe (O'Day *et al.*, 2004), no Fe nearest neighbor is present in SWy-2 (Vantelon *et al.*, 2003). Furthermore the FeO_6 octahedron in SWy-2 is less distorted than in IMt-1. IMt-1 has been shown to be a good proxy for Fe(III) bound in micaceous minerals (O'Day *et al.*, 2004).

Two-line ferrihydrite is a poorly crystalline Fe oxyhydroxide which is commonly formed in pedogenic environments (Cornell & Schwertmann, 2003; Rancourt *et al.*, 2005). Ferrihydrite and its varieties are also formed under biological control (e.g. ferritin, b-HFO). 2-line ferrihydrite serves as a proxy for the class of Fe (oxyhydr-)oxides (O'Day *et al.*, 2004).

Table S1. Fe reference compounds used for the linear combination fitting

name	group	Fe/Me_o[§] (%)	Fe(II) (%)	type	beamline	source
biotite	Fe(II)-ps	71	87[†]	natural	HASYLAB A1	isolate from granite obtained from M. Kiczka
chlorite (CCa-2)	Fe(II)-ps	52	91[†]	natural	HASYLAB C	Source Clay Repository
smectite (SWy-2)	Fe(III)-ps	15	7[‡]	natural	HASYLAB C	Source Clay Repository
illite (IMt-1)	Fe(III)-ps	21	12[†]	natural	HASYLAB C	Source Clay Repository
2-line ferrihydrite	ox	-	0[*]	synthetic	HASYLAB A1	
goethite	ox	-	0[*]	synthetic	ANKA XAS	obtained from O. Jacquat
maghemite	ox	-	0[*]	synthetic	HASYLAB A1	obtained from J. Wiederhold
magnetite	ox	-	33[*]	natural	HASYLAB A1	isolate form granite obtained from M. Kiczka
siderite	carb	-	100[*]	natural	ANKA XAS	obtained from mineral collection of ETH Zurich
pyrite	sulfide	-	100[*]	natural	ANKA XAS	obtained from mineral collection of ETH Zurich
FeS	sulfide	-	100[*]	chemical	ANKA XAS	Fluka 44995
$Fe(II)SO_4(aq)$	Fe(II) (aq)	-	100[*]	chemical	ANKA XAS	

Abbreviations: ps: phyllosilicate; ox: oxide / oxyhydroxide; carb: carbonate; rep: repository.
[§]amount of Fe divided by the total amount of cations in the octahedral sheet; this fraction was approximated by the Fe/(Fe+Mg) ratio for the Fe(II)-ps samples and the $Fe/(Fe+Al_{oct})$ ratio for the Fe(III)-ps samples. The data are derived from own XRF measurements (Fe(II)-ps) and from the stoichiometric data given by Vantelon et al., 2003 (Fe(III)-ps), respectively. [†]Estimated from pre-edge barycenter position according to a method described by Wilke et al., 2001. [‡] No high energy resolution data were available for an experimental determination. Thus the Fe(II) content of SWy-2 was estimated by using the stoichiometric data given in Vantelon et al., 2003. [*]deduced from the stoichiometry.

S3 X-ray diffraction analysis of the topsoil sample

XRD patterns were recorded on a Bruker D4 diffractometer (Cu anode, energy dispersive solid state detector; continuous scans from 4° to 70° 2θ with variable slits). The diffraction pattern was background subtracted and sample height displacement was corrected by aligning the Quartz diffraction pattern in the sample to the one of a standard sample (powder diffraction pattern 00-046-1045).

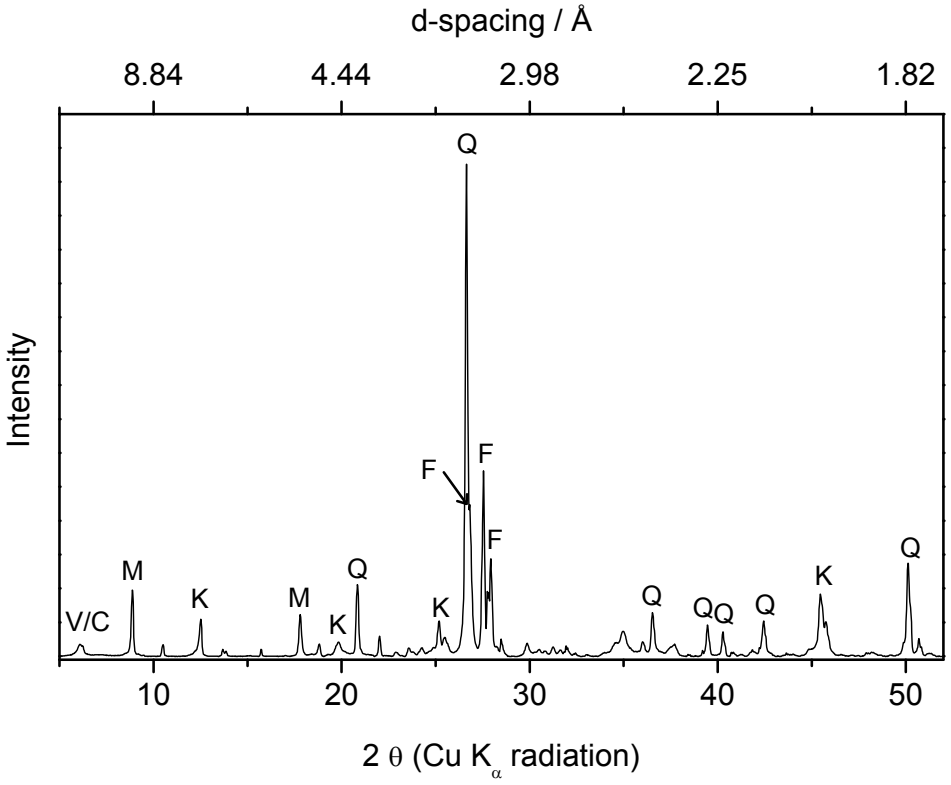

Figure S1. Powder X-ray diffraction pattern of the bulk topsoil sample; M: mica; K: kaolinite; Q: quartz; F: feldspar (Albite, Orthoclase); C: chlorite; V: vermiculite.

S4 Fe K-edge XANES LCF

Figure S2 contains the smoothed first derivative spectra of the samples and references shown in Figure 1. The linear combination fits to the normalized XANES spectra were in general similar to the fit to the first derivative XANES spectra, in that the fitted fractions agreed within about 10% (absolute). Only for the bulk and the matrix spectrum the results of the two approaches differed distinctly. We will briefly discuss the case of the bulk spectrum. The biotite, IMt-1, SWy-2, and 2L-Fh fractions resulting from the fit to the normalized XANES spectrum of the bulk soil were 24%, 40%, 36%, and 0%, respectively. Thus, particularly the SWy-2 and the 2L-Fh fraction differed distinctly between the fits to the derivative and the normal XANES spectrum (normal: SWy-2: 36%, 2L-Fh: 0%; derivative: SWy-2: 2%, 2L-Fh: 29%). As the references did not provide an exact reproduction of the sample spectrum, these differences reflect the different sensitivities of the two approaches; while the fit to the normal spectrum provides a better absolute match particularly in the region of the post-edge peak around 7145 eV, the fit to the derivative spectra better reproduced the overall structure in the XANES spectrum. For our purposes we preferred the latter fit, as the reproduction of the spectral shape ensures that the full spectrum of bonding environments is reflected in the fit, while the intensity can also be influenced by experimental factors of subtle characteristics of the Fe species in the sample which are not reproduced in the reference spectra.

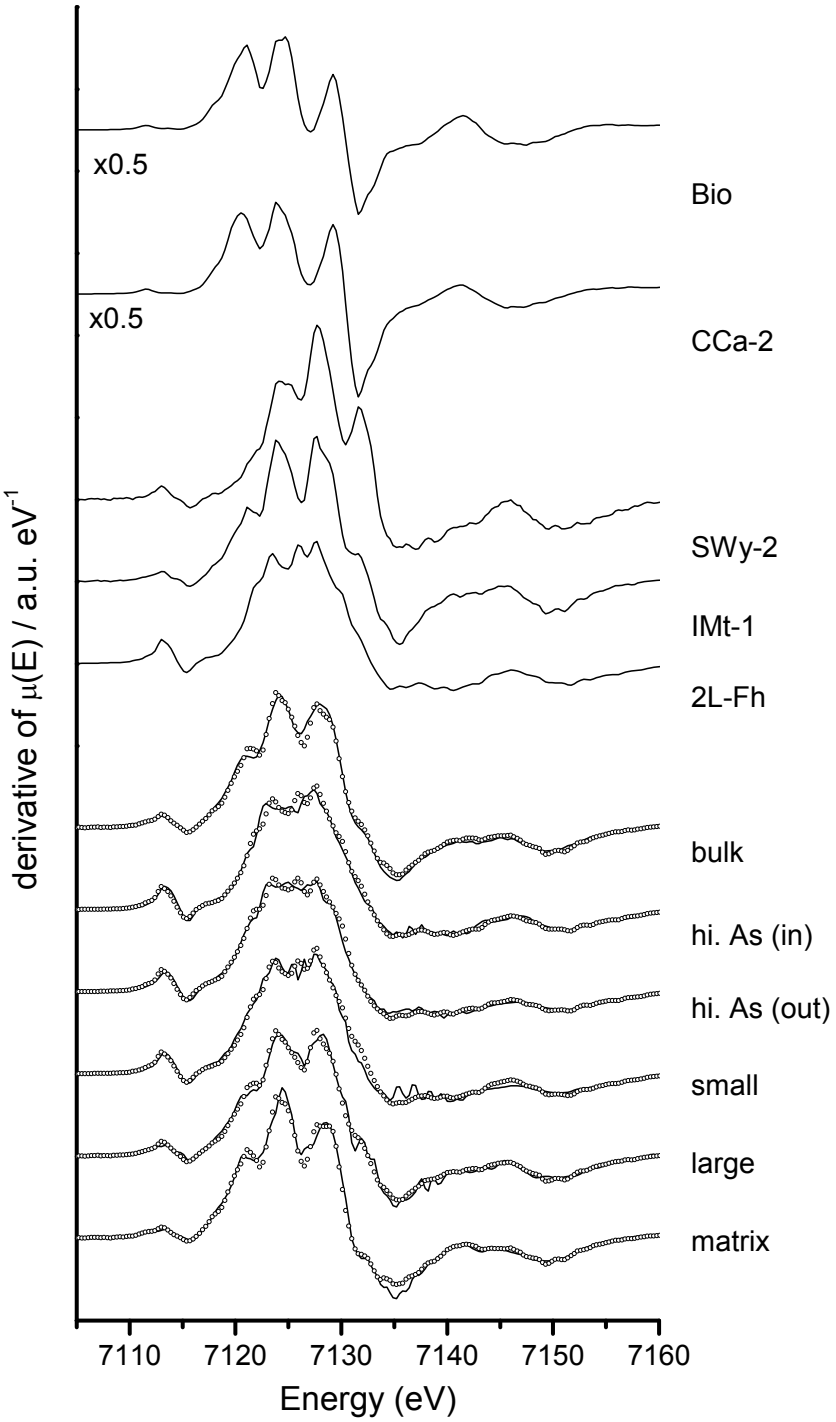

Figure S2. smoothed first derivative of the normalized sample and reference XANES spectra shown in Figure 1. The derivative spectra of Bio and CCa-2 were scaled by 0.5. In addition the LCF fits to the sample spectra are shown (open dots).

S5 Additional figures

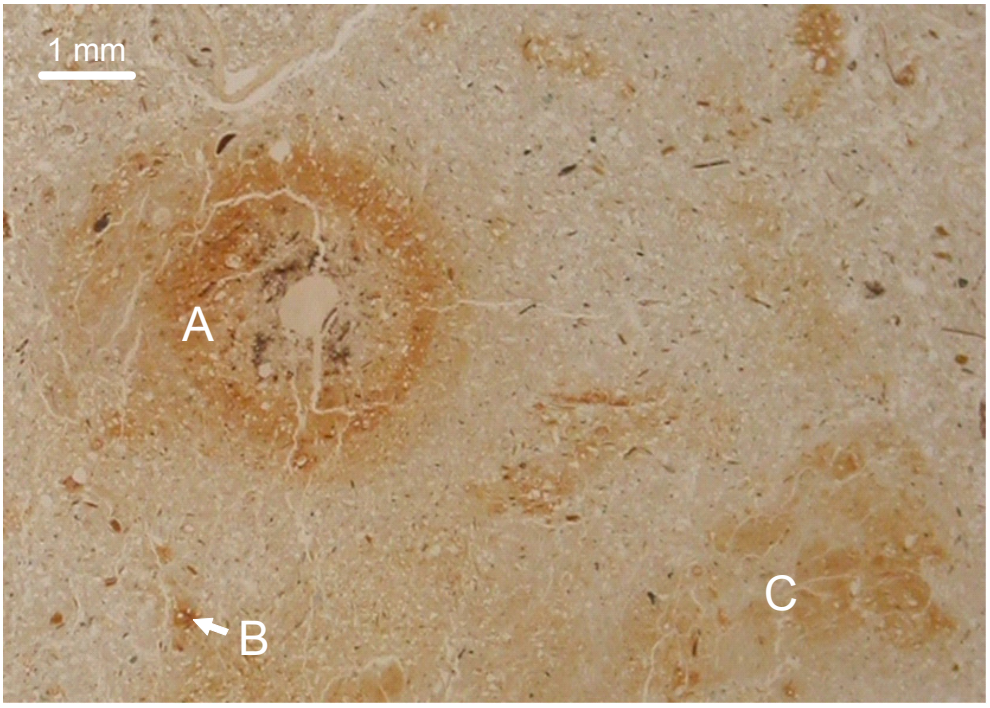

Figure S3. Light microscope image of a soil thin section showing a large (A) and a small (B) concentric element enrichment pattern and a diffuse accumulation of Fe(III) precipitates (C). An approximate scale bar is shown.

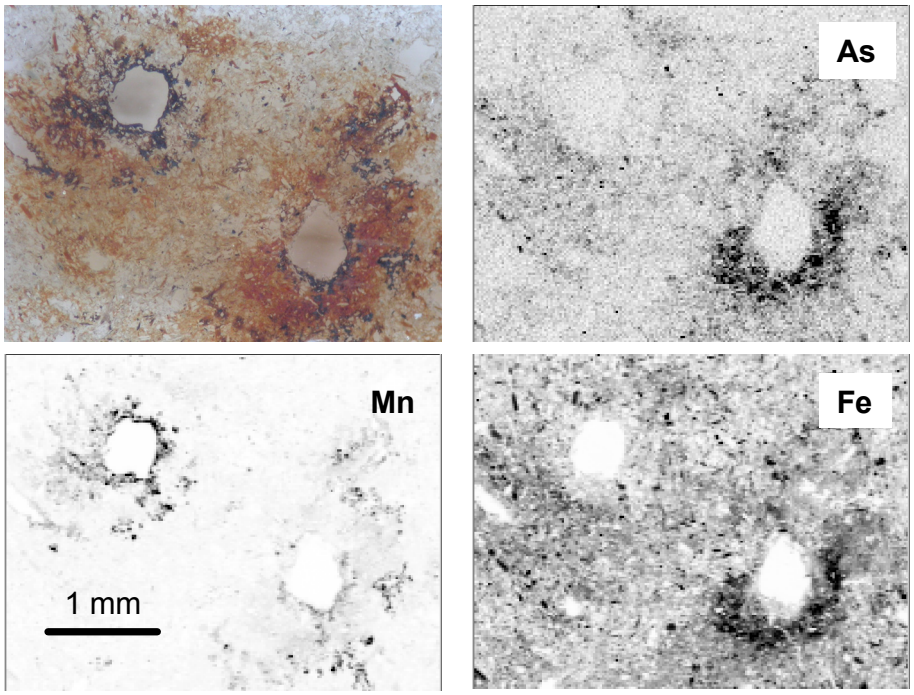

Figure S4. Light microscope image (top left) of two larger (root) channels, along with the distribution of As, Fe, and Mn (μ-XRF). The sample was collected in a depth between 14 and 16 cm in May 2006.

Literature cited

Cornell, R.M. & Schwertmann, U. 2003. *The Iron Oxides*. Wiley-VCH.

Dittmar, J., Voegelin, A., Roberts, L.C., Hug, S.J., Saha, G.C., Ali, M.A., Badruzzaman A.B.M. & Kretzschmar R. 2007. Spatial distribution and temporal variability of arsenic in irrigated rice fields in Bangladesh. 2. Paddy soil. *Environmental Science & Technology*, **41,** 5967-5972.

Drodt, M., Trautwein, A.X., König, I., Suess, E. & Bender Koch, C. 1997. Mössbauer spectroscopic studies on the iron forms of deep-sea sediments. *Physics and Chemistry of Minerals*, **24,** 281-293.

Elam, W.T., Ravel, B.D. & Sieber, J.R. 2002. A new atomic database for X-ray spectroscopic calculations. *Radiation Physics and Chemistry*, **63,** 121-128.

Jacquat, O., Voegelin, A., Villard, A., Marcus, M.A. & Kretzschmar, R. 2008. Formation of Zn-rich phyllosilicate, Zn-layered double hydroxide and hydrozincite in contaminated calcareous soils. *Geochimica et Cosmochimica Acta*, **72,** 5037-5054.

Krause, M.O. 1979. Atomic radiative and radiationless yields for K-shells and L-shells. *Journal of Physical and Chemical Reference Data*, **8,** 307-327.

O'Day, P.A., Rivera, N., Root, R. & Carroll, S.A. 2004. X-ray absorption spectroscopic study of Fe reference compounds for the analysis of natural sediments. *American Mineralogist*, **89,** 572-585.

Rancourt, D.G., Thibault, P.J., Mavrocordatos, D. & Lamarche, G. 2005. Hydrous ferric oxide precipitation in the presence of nonmetabolizing bacteria: Constraints on the mechanism of a biotic effect. *Geochimica et Cosmochimica Acta*, **69,** 553-577.

Vantelon, D., Montarges-Pelletier, E., Michot, L.J., Briois, V., Pelletier, M. & Thomas, F. 2003. Iron distribution in the octahedral sheet of dioctahedral smectites. An FeK-edge X-ray absorption spectroscopy study. *Physics and Chemistry of Minerals*, **30,** 44-53.

Voegelin, A., Weber, F.-A. & Kretzschmar, R. 2007. Distribution and speciation of arsenic around roots in a contaminated riparian floodplain soil: Micro-XRF element mapping and EXAFS spectroscopy. *Geochimica et Cosmochimica Acta*, **71,** 5804-5820.